

Four-dimensional data assimilation experiments with International Consortium for Atmospheric Research on Transport and Transformation ozone measurements

Tianfeng Chai,¹ Gregory R. Carmichael,¹ Youhua Tang,¹
 Adrian Sandu,² Michael Hardesty,³ Peter Pilewskie,⁴ Sallie Whitlow,⁵
 Edward V. Browell,⁶ Melody A. Avery,⁶ Philippe Nédélec,⁷ John T. Merrill,⁸
 Anne M. Thompson,⁹ and Eric Williams¹⁰

Received 6 July 2006; revised 2 March 2007; accepted 19 March 2007; published 26 May 2007.

[1] Ozone measurements by various platforms during the International Consortium for Atmospheric Research on Transport and Transformation (ICARTT) operations in the summer of 2004 are assimilated into the STEM regional chemical transport model (CTM). Under the four-dimensional variational data assimilation (4D-Var) framework, the model forecast (background) error covariance matrix is constructed using both the so-called NMC (National Meteorological Center, now National Centers for Environmental Prediction) method and the observational (Hollingworth-Lönnberg) method. The inversion of the covariance matrix is implemented using truncated singular value decomposition (TSVD) approach. The TSVD approach is numerically stable even with severely ill conditioned vertical correlation covariance matrix and large horizontal correlation distances. Ozone observations by different platforms (aircraft, surface, and ozonesondes) are first assimilated separately. The impacts of the various measurements are evaluated on their ability to improve the predictions, defined as the information content of the observations under the current framework. In the end, all observations are assimilated into the CTM. The final analysis matches well with observations from all platforms. Assessed with all the observations throughout the boundary layer and midtroposphere, the model bias is reduced from 11.3 ppbv for the base case to -1.5 ppbv. A reduction of 10.3 ppbv in root mean square error is also seen. In addition, the potential of improving air quality forecasts by chemical data assimilation is demonstrated. The effect of assimilating ozone observations on model predictions of other species is also shown.

Citation: Chai, T., et al. (2007), Four-dimensional data assimilation experiments with International Consortium for Atmospheric Research on Transport and Transformation ozone measurements, *J. Geophys. Res.*, 112, D12S15, doi:10.1029/2006JD007763.

1. Introduction

[2] Similar to numerical weather predictions (NWPs), an improvement in air quality analyses and forecasts requires integration with observations to constrain the model. This is known as data assimilation. Experiments in NWPs have shown that advanced data assimilation such as four-dimensional variational data assimilation (4D-Var) are more

effective than the traditional techniques such as nudging and Optimal Interpolation (OI). Compared to NWPs, there is much less experience in chemical data assimilation.

[3] Fisher and Lary [1995] first applied 4D-Var data assimilation to the analysis of chemically active trace species using a Lagrangian model. Elbern *et al.* [1997, 2000], Elbern and Schmidt [1999, 2001], and Hoelzemann *et al.* [2001] developed a 4D-Var chemical data assimilation system using a regional Eulerian model, European Air pollution Dispersion model (EURAD). Improvements in

¹Center for Global and Regional Environmental Research, University of Iowa, Iowa City, Iowa, USA.

²Department of Computer Science, Virginia Polytechnic Institute and State University, Blacksburg, Virginia, USA.

³Environmental Technology Laboratory, NOAA, Boulder, Colorado, USA.

⁴NASA Ames Research Center, Moffett Field, California, USA.

⁵Climate Change Research Center, Institute for the Study of Earth, Oceans, and Space, University of New Hampshire, Durham, New Hampshire, USA.

Copyright 2007 by the American Geophysical Union.
 0148-0227/07/2006JD007763

⁶NASA Langley Research Center, Hampton, Virginia, USA.

⁷Laboratoire d'Aérolologie, Centre National de la Recherche Scientifique, Toulouse, France.

⁸Center for Atmospheric Chemistry Studies, Graduate School of Oceanography, University of Rhode Island, Narragansett, Rhode Island, USA.

⁹NASA Goddard Space Flight Center, Greenbelt, Maryland, USA.

¹⁰Chemical Sciences Division, Earth System Research Laboratory, NOAA, Boulder, Colorado, USA.

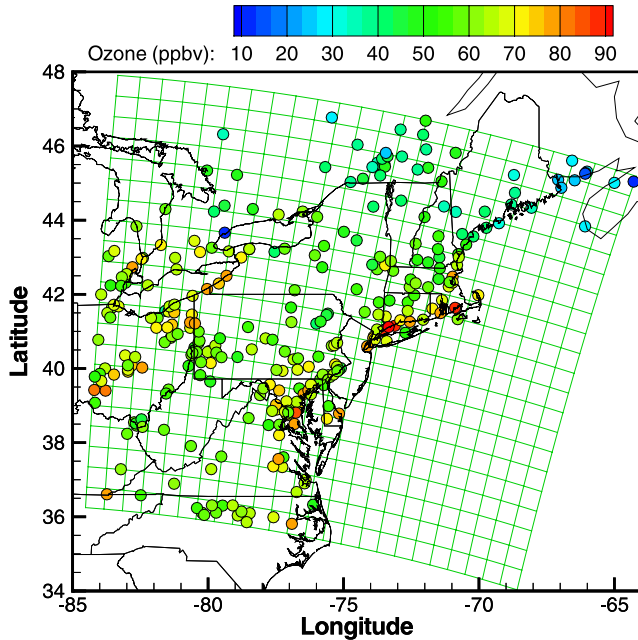


Figure 1. Computational grid and AIRNOW stations (color coded by ozone measurements at 1900 UT on 20 July 2004).

ozone forecasts subsequent to the assimilation procedure was found [Elbern and Schmidt, 2001]. Using the 4D-Var approach with the regional CTM STEM-2K1 (Sulfur Transport Eulerian Model, version 2K1) [Daescu and Carmichael, 2003; Carmichael et al., 2003; Sandu et al., 2005], Chai et al. [2006] showed improvement of analyses by assimilating flight measurements of various chemical species. In previous studies, the model error covariance matrices were not specifically investigated, although it is well known that this will greatly affect the data assimilation results.

[4] Coordinated measurements were made by the International Consortium for Atmospheric Research on Transport and Transformation (ICARTT) consortium during the 2004 study in northeastern United States and the Maritime Provinces of Canada. These measurements provide invaluable information in evaluating and improving air quality models and model forecasts [Singh et al., 2006]. The rich set of observations and extensive model studies during ICARTT make this period well suited for data assimilation experiments, and an ideal setting, to test the advanced chemical data assimilation framework, to generate better analyses using both observations and model results, and to investigate the potential to improve the future of air quality forecasts.

[5] In this paper we focus on the use of the ICARTT ozone measurements from different sources to improve the predicted ozone distributions. We demonstrate how the modeling and measurement activities of ICARTT can be used in the data assimilation framework. We specifically demonstrate that the model forecast (background) error covariance matrix can be constructed using the air quality forecasts during the ICARTT field experiments. Then we introduce a truncated singular value decomposition regularization (TSVD) technique to implement the error correlation matrix in the analysis. We also systematically evaluate the

information content of measurements from different platforms by assimilating them separately and comparing the predictions to withheld observations. A final analysis is performed with all the observations assimilated into the regional CTM. The effects of the data assimilation on model predictions of other species, and on the chemical forecasts after the data assimilation period are also discussed.

[6] The paper is organized as the following. A brief description of the STEM model and the variational data assimilation procedure is given in section 2. Section 3 describes the model setup and the observations to be assimilated. Section 4 discusses how the model error covariance is generated and implemented into the current 4D-Var system. Data assimilation experiments are presented and discussed in section 5. A summary is given in section 6.

2. Method

2.1. STEM

[7] In this study, we employed the STEM-2K3 [Tang et al., 2004] regional chemical transport model. The STEM-2K3 model is a flexible regional-scale chemical transport model using SAPRC99 chemical mechanism [Carter, 2000] with online photolysis solver [Tang et al., 2003]. Meteorological inputs to the model came from the fifth-generation Mesoscale Model (MM5) using the Aviation model (AVN) during forecasting and NCEP (National Centers for Environmental Prediction) FNL (Final Global Data Assimilation System) analyzed data during postanalysis. During forecasting, the STEM-2K3 was run over three nested domains subsequently. The first domain covers the continental United States. A grid with a 60 km horizontal resolution (62 cells in longitude, and 97 cells in latitude) was used over this domain. Vertically the model had 21 layers, extending from the surface to 100 hPa using 0.999, 0.9965, 0.9925, 0.985, 0.97, 0.945, 0.91, 0.87, 0.825, 0.77, 0.71, 0.65, 0.59, 0.53, 0.47, 0.41, 0.35, 0.285, 0.21, 0.125, and 0.04 in sigma coordinate. The boundary conditions are provided by the MOZART global chemical model predictions, i.e., MOZART GFDL (NOAA GFDL) [Horowitz et al., 2003] during the forecast, and MOZART NCAR [Pfister et al., 2005] during postanalysis. MOZART NCAR assimilated CO values from MOPITT (Measurements of Pollution in the Troposphere instrument on board the TERRA satellite). The Grell cumulus parameterization [Grell et al., 1994] and the medium-range forecast (MRF) planetary boundary layer parameterization [Hong and Pan, 1996] were used for the MM5 runs. The emissions inventory was based on the U.S. EPA National Emissions Inventory NEI 2001, with updated

Table 1. Ozone Observations on 20 July 2004

Observations	Description
AIRNOW	EPA surface stations, hourly averaged data used
DC3	vertical profile of ozone mixing ratio from lidar
MOZ-FN	MOZAIC, Frankfurt–New York flight
MOZ-NF	MOZAIC, New York–Frankfurt flight
P3	NOAA P3-B measurement
AIRMAP	UV SPECTROSCOPY measurement at four sites
DC8-In	NASA in situ ozone via nitric oxide chemiluminescence
DC8-Li	DC-8 composite tropospheric ozone cross sections
RHODE	ozonesonde/radiosonde data from Narragansett, RI
RONBR	ozonesonde/radiosonde data from the R/V <i>Ronald H. Brown</i>

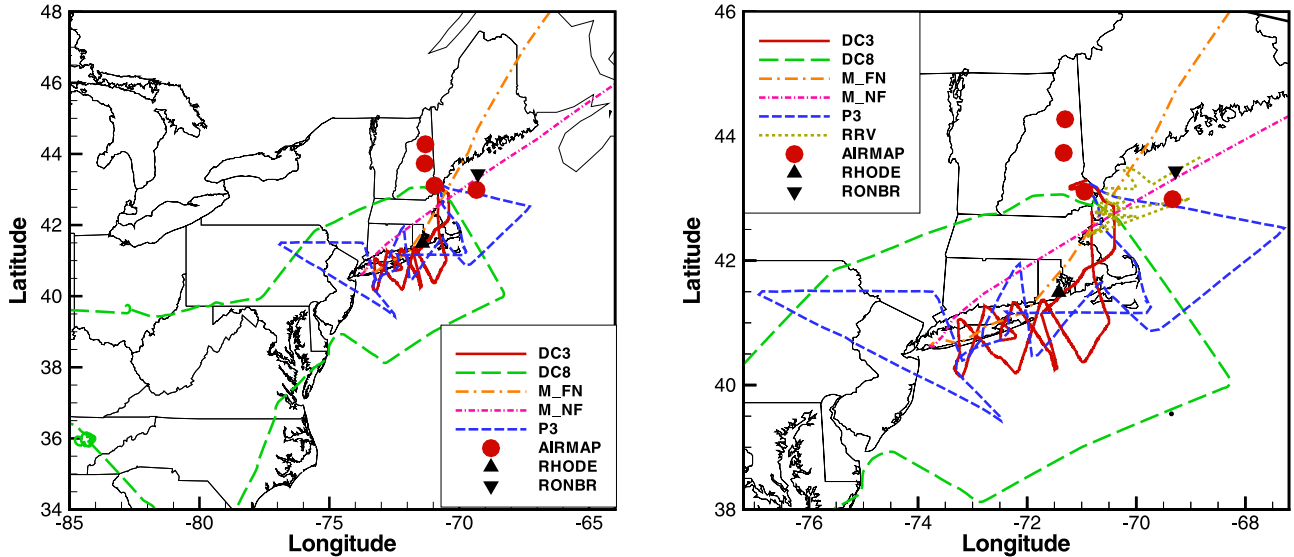


Figure 2. Flight tracks, AIRMAP stations, and ozonesonde locations. RRV: positions of NOAA research vessel *Ronald H. Brown* between 1200 UT on 20 July to 1200 UT on 22 July 2004.

large point source emissions (Gregory Frost at NOAA Earth Systems Research Laboratory, personal communication). Upper troposphere lightning NO_x emissions were added to the model based on the National Lightning Detection Network (NLDN), modulated by signal strength and multiplicity of flashes. Further information about the lightning emissions is given by Tang *et al.* [2007]. Biogenic emissions were estimated using Biogenic Emissions Inventory System 2 (BEIS2) which generates time-varied isoprene and monoterpene emissions driven by meteorological variables from MM5. Forest fires that occurred during the ICARTT period were largely outside the model domain (in Alaska and Northwestern Canada), therefore their influence was incorporated through lateral boundary conditions from MOZART global chemical model predictions.

2.2. STEM 4D-Var System

[8] The current 4D-Var data assimilation system includes a regional CTM, i.e., the STEM, its adjoint model, and a minimization routine. Here we briefly describe the system, and the readers are referred to Chai *et al.* [2006] for further details.

[9] The evolution of the chemical constituent concentration vector c in time (t) is described as

$$\frac{\partial c}{\partial t} = -u \cdot \nabla c + \frac{1}{\rho} \nabla \cdot (\rho K \cdot \nabla c) + \frac{1}{\rho} f + E \quad (1)$$

Here we denote by u the wind field vector, ρ the air density, K the turbulent diffusivity tensor, f the chemical transformation rate, and E the rate of elevated emissions.

[10] The adjoint of the tangent linear model of the STEM-2K1 defines the evolution of the adjoint variable vector λ , which reads as

$$\frac{\partial \lambda}{\partial t} + \nabla \cdot (u \lambda) = -\nabla \cdot \left(\rho K \cdot \nabla \frac{\lambda}{\rho} \right) - (F \cdot \lambda) - \phi \quad (2)$$

In this equation ϕ is a forcing functional vector and will be defined later. F is a tensor function, obtained by linearizing the incremental f as $\delta f \approx F \cdot \delta(\rho c)$. As f is a nonlinear function of (ρc) , F also varies with (ρc) , i.e., $F = F(\rho c)$. This implies that the forward model must be first solved, the state $c(x, t)$ saved for all t , then the adjoint model can be integrated backward in time from T down to t^0 .

[11] The 4D-Var system seeks the optimal solution which minimizes the cost functional J , defined as

$$J = \frac{1}{2} [c_0 - c_b]^T B^{-1} [c_0 - c_b] + \frac{1}{2} [y - h(c)]^T O^{-1} [y - h(c)] \quad (3)$$

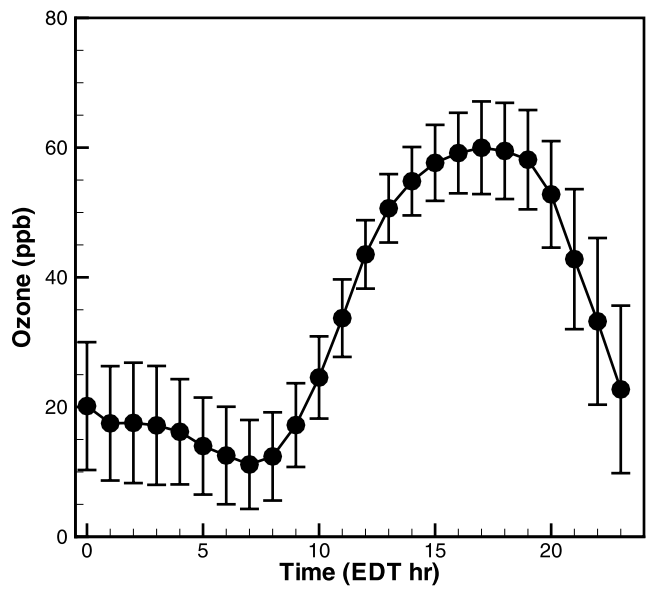


Figure 3. Domain-averaged AIRNOW ozone concentration and standard deviation inside a grid cell on 20 July 2004.

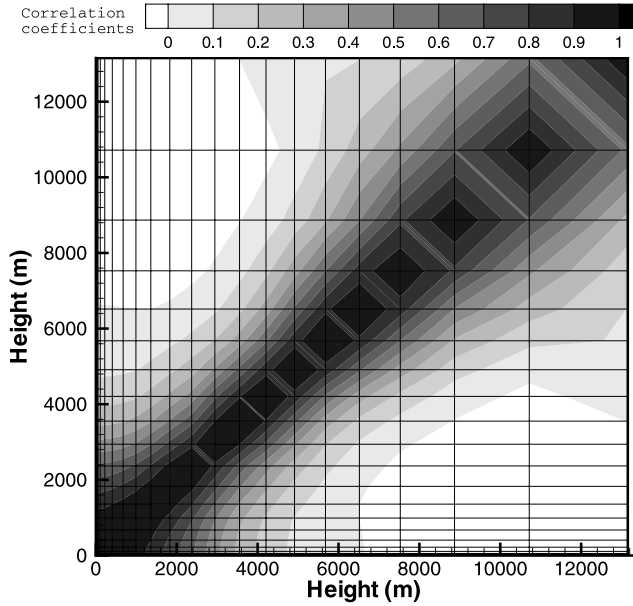


Figure 4. Model error correlation coefficients between vertical levels. The nonuniform vertical grid is indicated by the height of each level, shown as the mesh in the plot.

where B and O are error covariance matrices for a priori model forecast (background) and observations in discrete spaces, respectively. h is a projection operator, calculating the observation vector $y = y(x, t)$ from the model space $c = c(x, t)$. In the current study the initial concentrations $c_0 = c(t = 0)$ are chosen as the only control parameters to adjust, though in principle any model parameters including emissions can be adjusted. Hereafter, the subscript “0” is used to denote variables at the instant $t = 0$. Assuming that the operator h is linear, $h(c)$ can be written as $h(c) = H \cdot c$. In our

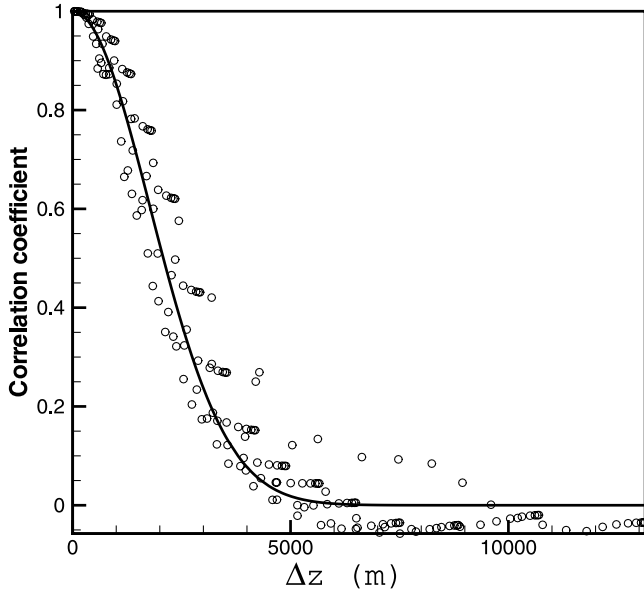


Figure 5. Model error correlation coefficients between vertical levels, as a function of Δz , the distance between two levels. The line indicates $e^{-\frac{\Delta z}{l_z^2}}$, where $l_z = 2500$ m.

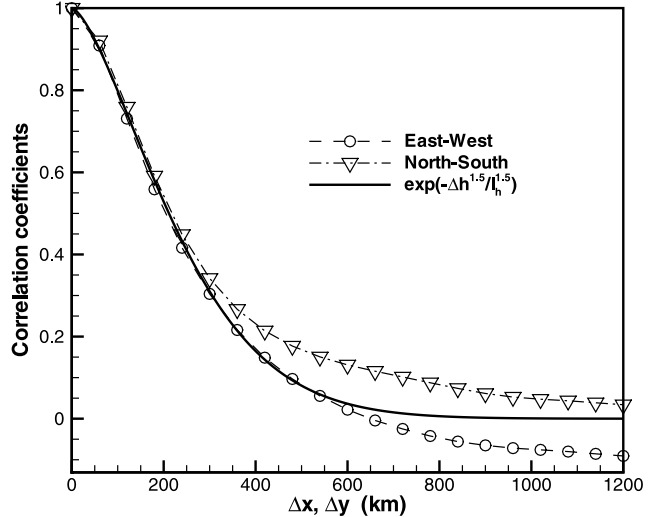


Figure 6. Model error correlation coefficients as a function of horizontal distance Δx or Δy . They can be fitted by $e^{-\frac{\Delta h^{1.5}}{l_h^{1.5}}}$, where $l_h = 270$ km.

application, H reflects trilinear interpolation in space and linear interpolation in time when constructing model counterparts of the observations. It is also represented in the H transformation matrix.

[12] The forcing term ϕ in equation (2) appears as

$$\phi = H^T \cdot O^{-1} \cdot [y - H \cdot c] \quad (4)$$

The backward integration of equation (2) gives adjoint variables at any time, which are the sensitivities of the cost functional with respect to state variables (concentrations), i.e.,

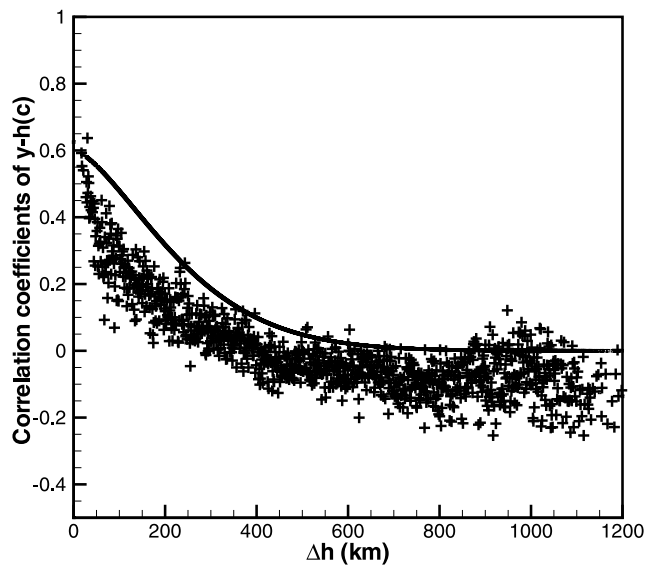


Figure 7. Correlation coefficients of observational increments between AIRNOW stations, as a function of the horizontal distance (Δh) between stations. The distance increment is 1 km, within which the average correlation of multiple station pairs is shown. The line shown is $R_z e^{-\frac{\Delta h^{1.5}}{l_h^{1.5}}}$, where $l_h = 270$ km and $R_z = 0.6$.

Table 2. Maximum and Minimum Singular Values, Condition Number, Rank p in TSVD Regularization, and Singular Value σ_p of Spatial Correlation Matrices X , Y , and Z

Matrix	Size ($n \times n$)	σ_1	σ_n	Condition Number	p	σ_p
X	25×25	7.49	2.65×10^{-2}	283	14	7.57×10^{-2}
Y	22×22	7.35	2.65×10^{-2}	277	12	8.35×10^{-2}
Z	21×21	9.97	7.69×10^{-17}	1.30×10^{17}	8	1.18×10^{-1}

$$\delta J = \lambda^T \cdot \delta c \quad (5)$$

Note that the background part of the cost functional in equation (3) adds one more term to the gradient of the cost functional with respect to initial concentrations. Using equation (3), we have

$$\delta J = [\lambda_0^T + (c_0 - c_b)^T \cdot B^{-1}] \cdot \delta c_0 \quad (6)$$

where $\lambda_0^T + (c_0 - c_b)^T \cdot B^{-1}$ is the gradient information needed for the minimization. The optimal initial condition c_0 can be found efficiently by applying many different minimization routines. Quasi-Newton limited memory L-BFGS [Byrd et al., 1995] is used by most 4D-Var applications. In this article, an updated version, L-BFGS-B [Zhu et al., 1997] is used. [Chai et al., 2006] found that adding bound constraints improved the computation efficiency. For the following data assimilation tests, the maximum number of iterations is set to be 25 in the minimization. In each iteration, both the STEM and its adjoint are run in the 4D-Var data assimilation time window.

3. Experiment Setup and Observations

[13] Figure 1 shows the computational domain for the following data assimilation experiments. A 60 km grid used

for 4D-Var assimilation is also shown. Note that we typically use a 12 km resolution for both forecasting and analysis for this domain when there is no 4D-Var calculation [Tang et al., 2007]. However, since the typical 25 4D-Var iterations add about 80 times to the computational time compared to the STEM forecast run, we focus on a 60 km grid, which is more representative of the resolutions of global models. The boundary conditions for this domain came from the 60 km grid covering the continental U.S. that was described in section 2.1.

[14] We selected the data assimilation time window to be 12 hours, which is 1200–2400 UT, on 20 July 2004. The date was chosen because it was a day with a high density of observations. The time window covers daytime peak ozone period, as well as the operational time of NOAA P3, NASA DC-8 flights, and two ozonesondes in the domain. During this time period there were ozone measurements by two MOZAIC (Measurements of Ozone and water vapour by in-service Airbus Aircraft, <http://mozaic.aero.obs-mip.fr>) flights [Thouret et al., 1998; Marenco et al., 1998; Nédélec et al., 2003]. Most of the NOAA DC3 flight was also in the chosen time window. The ozone measurements during this period used in the data assimilation experiments are listed in Table 1. The locations of the AIRNOW measurements are shown in Figure 1. Figure 2 shows the flight tracks, the locations of the AIRMAP measurements, and the ozone-sonde locations.

[15] The CTM time step is 15 min. With operator splitting, during each time step, transport in each direction is processed twice and the chemistry is solved using a Rosenbrock method [Sandu et al., 2003; Daescu et al., 2003]. The measurements contain more temporal and spatial variation than the model can resolve at the current resolutions. For instance, Figure 1 shows that the ozone measurements from different monitoring sites inside one grid cell can vary by as much as 30 ppbv. Such variation is called representative error. In the data assimilation framework, it is

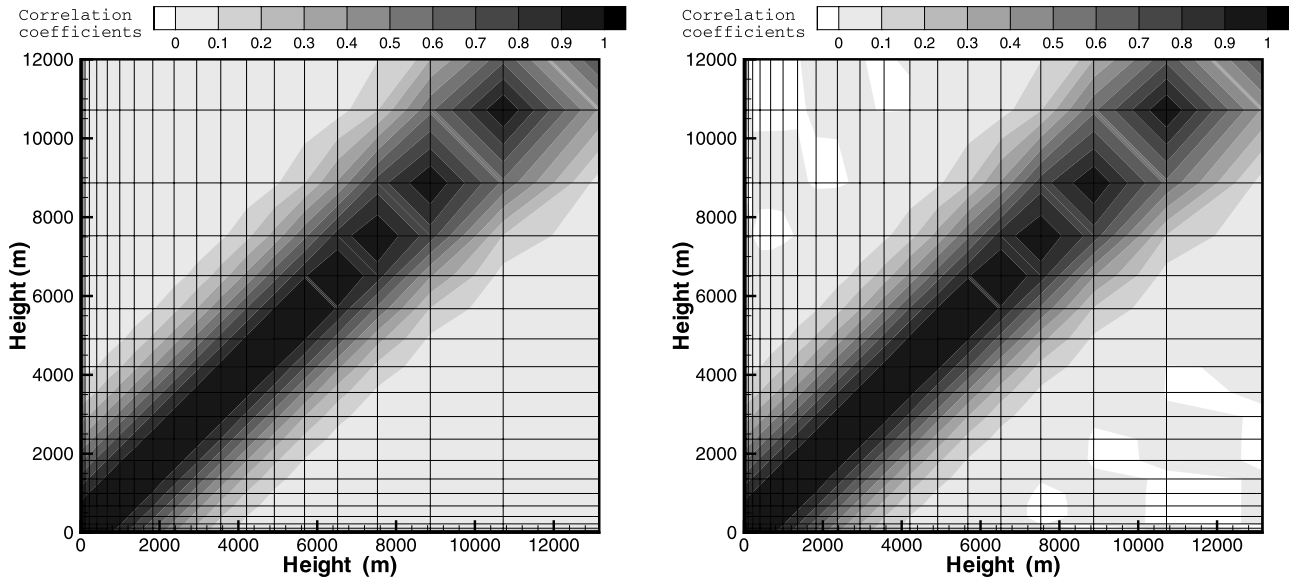


Figure 8. Vertical correlation of model errors, (left) Z and (right) Z_q . Z is used to approximate the correlation calculated through the NMC approach, shown in Figure 4. Z_q is after TSVD regularization. The nonuniform vertical grid is indicated by the height of each level, shown as the mesh in the plot.

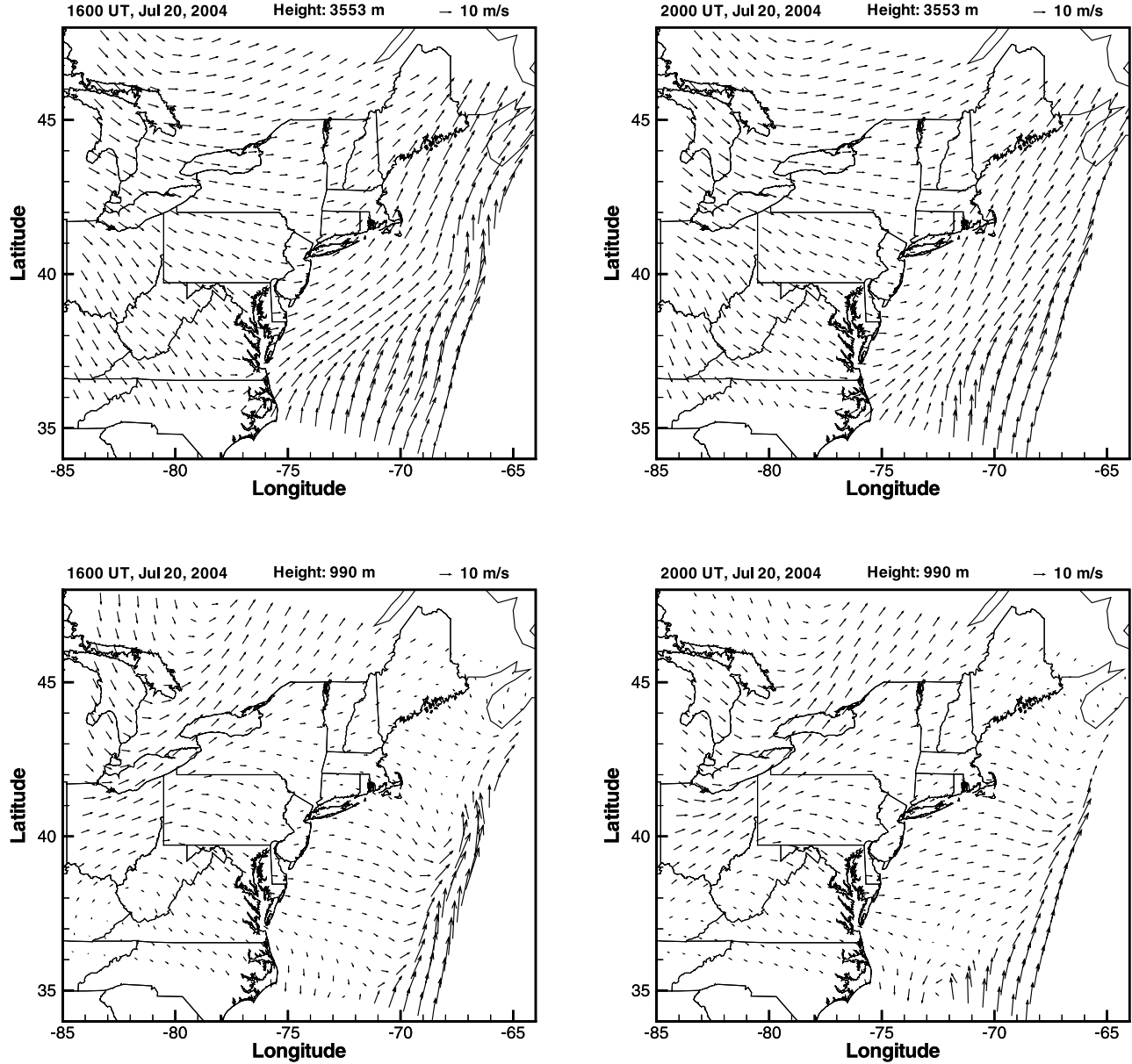


Figure 9. Wind fields at 1600 UT and 2000 UT, at $h = 990$ m and 3553 m.

necessary to account for the observational errors which include both the measurement errors and the representative errors. As the representative error is normally much larger than the measurement error [Daley, 1991], we choose to neglect the measurement error and use the standard deviation of ozone measurements within a grid cell as a measure of the representative error. Figure 3 shows the hourly domain-averaged AIRNOW ozone measurements and standard deviations inside a grid cell. It is seen that the standard deviation varies from a maximum value of ≈ 13 ppbv at night to ≈ 5 ppbv during the day. In the following data assimilation experiments we neglect the diurnal variations and assume a constant observational error of 8 ppbv. We also assume O in equation (3) is diagonal, i.e., no correlation between the observational errors. In addition, all the observations are processed according to the model resolution

by taking the averaged value inside each four-dimensional grid cell.

4. Model Forecast Error Covariance

4.1. NMC Results

[16] There are several methods to establish the model forecast error covariance matrices needed in the data assimilation procedure. One method is to use the NMC (National Meteorological Center, now National Centers for Environmental Prediction) approach [Parrish and Derber, 1992], which is used in operational data assimilation with NWPs. During the ICARTT field campaign, 3-day air quality forecasts using the STEM were initiated everyday. This resulted in three different forecasts for any specific time. Following the NMC method approach, model error covariance B in equation (3) can be calculated by substituting the

Table 3. Model Bias and RMS Error of the Base Run, Calculated Against Each Observation Platform^a

Error	AIRNOW	DC3	MOZ-FN	MOZ-NF	P3	AIRMAP	DC8-In	DC8-Li	RHODE	RONBR
Bias	15.3	16.0	1.8	4.2	9.8	13.8	-8.4	-3.8	3.7	9.4
RMS	26.3	22.8	20.7	15.3	18.3	19.9	18.6	17.9	13.4	24.3

^aUnit is ppbv. See Table 1 for descriptions of the observations.

model errors with the differences between forecasts. Specifically, we obtain model error samples at each point using

$$\epsilon_i = c^{f_i} - c^{\bar{f}} \quad (7)$$

where “i” is used to differentiate different forecasts.

[17] Unless spectral methods are used where the control variables form diagonal B matrices [Parrish and Derber, 1992], B matrices are often too large to store because of the correlation between model forecast errors. For instance, if only initial ozone concentrations are chosen as control parameters to be adjusted, the number of control variables is $N_x \times N_y \times N_z = 25 \times 22 \times 21 = 11,550$. This will result in a $11,550 \times 11,550$ B matrix that has 133,402,500 components. Not only the direct inverse of a large matrix is extremely expensive, the often rank-deficient B makes the inverse numerically unstable. Courtier [1997] and Lorenc [1997] proposed to change the control variables by preconditioning in order to avoid the direct inversion. Recently multidimensional recursive filters have been used to model error correlations [Gao et al., 2004; Purser et al., 2003a, 2003b]. However, it is difficult to apply the method to nonuniform grids such as the vertical grid used in the STEM, or complicated non-Gaussian covariances. Here we use singular value decomposition (SVD) that directly implement the covariances calculated from the NMC approach. To avoid storing the error covariance matrix explicitly, we assume B can be written as

$$B = X \otimes Y \otimes Z \otimes C \quad (8)$$

where X , Y , and Z are matrices of sizes $N_x \times N_x$, $N_y \times N_y$, and $N_z \times N_z$ and they represent the error correlation in three different directions. C is the error covariance matrix at a single grid point that represents both the error variances and correlation between different species. For the current case, C , as a scalar, is the background error variance for ozone only. \otimes denotes the Kronecker product [Horn and Johnson, 1991].

[18] The correlation coefficients are then calculated in three different directions. For instance, the model error correlation coefficients between two vertical levels are calculated as

$$R(k_1, k_2) = \frac{\overline{\epsilon_{k_1} \epsilon_{k_2}}}{\sqrt{\overline{\epsilon_{k_1}^2} \cdot \overline{\epsilon_{k_2}^2}}} \quad (9)$$

Here “ $\overline{\cdot}$ ” denotes the average over all grid points on the specific level. Also note that there are three samples of “errors” at each grid point, as calculated by equation (7). Figure 4 shows the correlation coefficients between vertical levels. The diagonal structure indicates that the correlation between two vertical levels can be approximated by $f(|z(k_1) - z(k_2)|)$. Assuming the correlation as a function of grid numbers, i.e., $f(|k_1 - k_2|)$, for such a nonuniform grid is not applicable here. Figure 5 shows the correlation as a function of the distance between two levels. We use a simple function $e^{-\frac{\Delta z^2}{l_z^2}}$, where the vertical length scale $l_z = 2500$ m, to approximate the vertical correlation. This function fits the actual NMC correlation results pretty well, as shown in Figure 5.

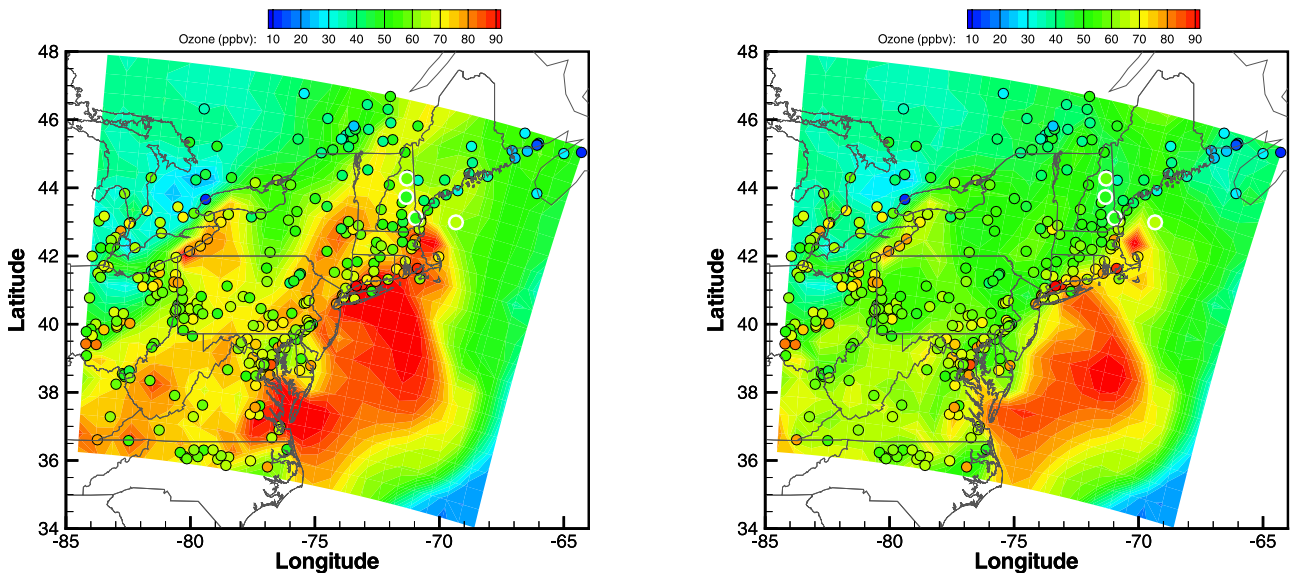


Figure 10. Predicted surface ozone concentrations at 2000 UT (1600 EDT) for (left) the base case and (right) case 9. AIRNOW and AIRMAP measurements are also indicated by the color-coded circles (slightly larger and white-outlined circles for AIRMAP).

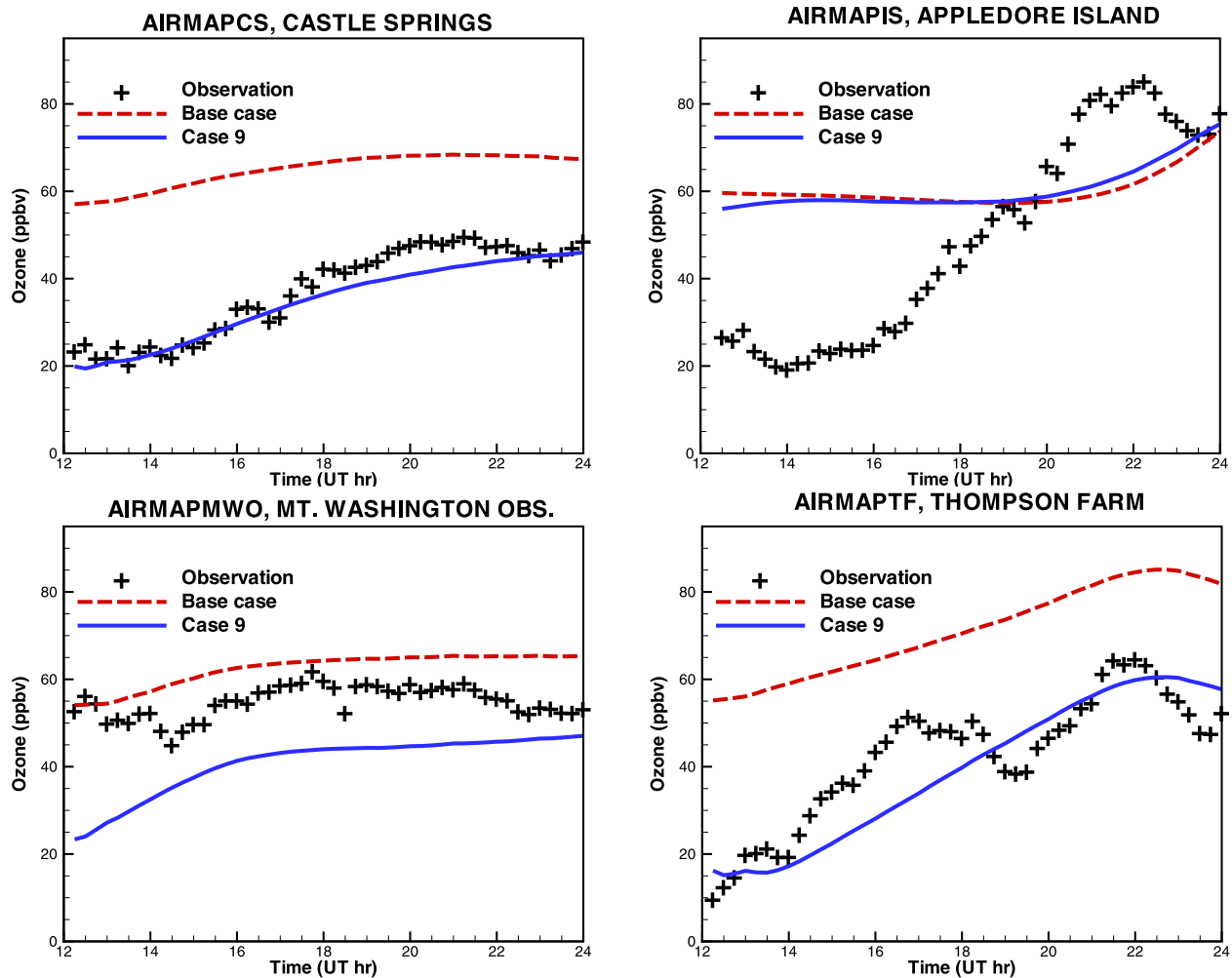


Figure 11. AIRMAP ozone observations and corresponding model predictions by the base case and case 9. Observations have been reduced according to model time resolution. Observations before 1600 UT are not assimilated.

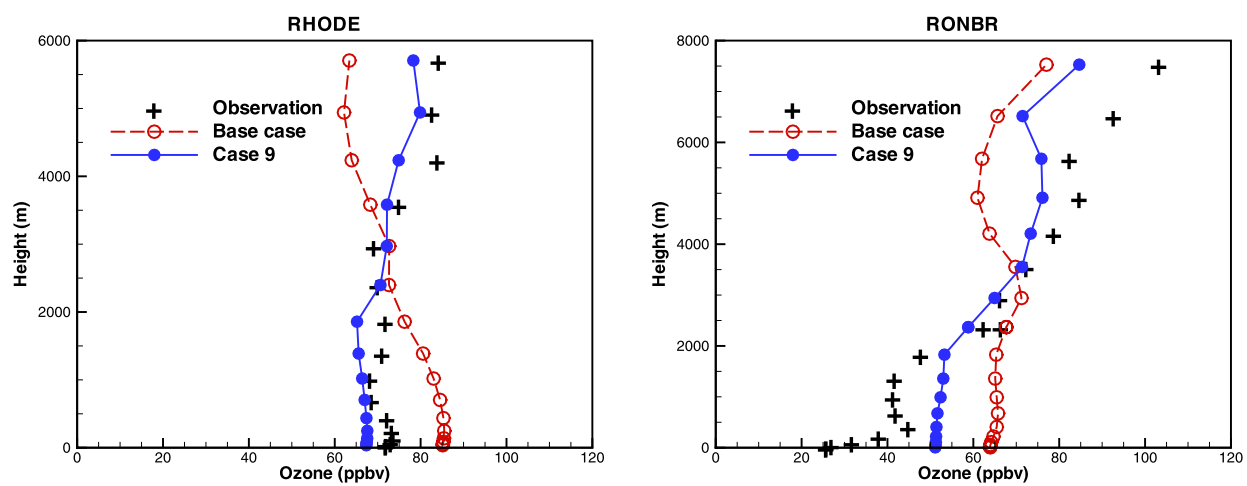


Figure 12. Ozone profiles by two ozonesondes (RHODE and RONBR) and corresponding model predictions by the base case and case 9. Observations have been reduced according to model resolutions, both in time and space.

Table 4. Descriptions of Data Assimilation Tests^a

Case	Assimilated Observations	Time	Number
1	AIRNOW	1300–2400 UT, hourly	2075
2	DC3	1852–2356 UT	412
3	MOZ-FN, MOZ-NF	1947–2007 UT, 2238–2252 UT	38
4	P3	1412–2207 UT	208
5	AIRMAP	1615–2400 UT	128
6	DC8-In	1416–2207 UT	138
7	DC8-Li	1429–2137 UT	465
8	RHODE, RONBR	1810–1822 UT, 1900–1921 UT	35
9	All above	1300–2400 UT	3499

^aListed observation time and number are after averaging the measurements inside each grid cell. Such averaging is extended to include the time dimension, which has a resolution of 15 min. See Table 1 for descriptions of the observations.

[19] Similarly, the correlation coefficients in two horizontal directions are calculated and plotted in Figure 6 as a function of the distances. It is seen that there is little difference in the two horizontal directions. They can be approximated by $e^{-\frac{\Delta h^{1.5}}{l_h^{1.5}}}$, where $l_h = 270$ km.

4.2. Background Error Variance Through Observational Method

[20] Another approach to calculate the background error covariance matrices is the observational method (Hollingworth-Lönnberg method) [Hollingsworth and Lönnberg, 1986; Daley, 1991]. It provides a more reliable estimate of the background error variance, as well as the ratio between the observation error variance and background error variance, which directly determines the weighting between the two terms in equation (3). However as the name implies, this method requires a substantially dense observational network.

[21] As shown in Figure 1, the dense coverage over the domain by the AIRNOW surface stations makes it suitable for the observational method. Using hourly observations during 20–22 July 2004 at each station, the correlation between the observational increment $y - h(c)$ at two stations i, j is calculated as

$$R_{ij} = \frac{\overline{(y^i - h^i(c))(y^j - h^j(c))}}{\sqrt{\overline{(y^i - h^i(c))^2} \cdot \overline{(y^j - h^j(c))^2}}} \quad (10)$$

where y is the observation and $h(c)$ is the model prediction before assimilation. “—” represents the average over time.

Table 5. RMS Error Changes of Model Predictions Against Each Observation Platform, Over the Base Case After Assimilation^a

Case	AIRNOW	DC3	MOZ-FN	MOZ-NF	P3	AIRMAP	DC8-In	DC8-Li	RHODE	RONBR
1	(−12.9)	−6.0	−4.0	4.0	−5.8	−6.7	−0.8	−0.7	−3.6	−3.3
2	−0.9	(−8.0)	−6.0	−2.4	−4.2	−3.8	−0.5	0.1	−2.3	−0.2
3	−0.3	−2.4	(−7.4)	(−4.9)	−1.2	0.0	−0.2	−0.2	−0.2	−0.1
4	−1.3	−5.9	−4.4	−3.0	(−7.4)	−2.9	−0.3	−0.4	−3.5	0.0
5	−0.6	−0.8	0.1	0.0	−0.9	(−9.5)	−0.5	0.0	−0.5	−1.1
6	−0.3	−0.7	−1.2	−0.1	−1.0	−3.3	(−6.1)	−1.4	−1.0	−0.6
7	−1.4	−2.3	−4.6	−2.8	−1.8	−0.2	−3.2	(−6.9)	−1.6	−0.3
8	−0.2	−0.2	−0.4	0.1	−0.2	0.0	−0.4	−0.2	(−6.4)	(−12.9)
9	−12.2	−7.0	−8.5	4.0	−7.3	−8.8	−6.9	−6.7	−8.5	−10.0

^aParentheses indicate observations of the platform have been assimilated in the data assimilation experiment. Unit is ppbv. See Table 4 for descriptions of the data assimilation tests.

R_{ij} are calculated between any two stations and the biases are removed such that R_{ij} is in the range of $[-1, 1]$.

[22] Figure 7 shows R_{ij} as a function of horizontal distance between station pairs. The zero intercept of the curve $R_z = \lim_{\Delta h \rightarrow 0} R(\Delta h) \approx 0.6$ measures the spatially correlated part (background error) of the total error, i.e.,

$$R_z = \frac{E_B^2}{E_B^2 + E_O^2} \quad (11)$$

Using this and $E_O = 8$ ppbv, E_B is estimated to be 10 ppbv. Note that $R(\Delta h)/R_z$ is an estimate of the horizontal background error correlation at ground level. The previously estimated horizontal correlation is also plotted in Figure 7 after being adjusted by R_z . They agree reasonably well. Compared with the correlation results from the NMC approach using all the levels, the correlation distance at ground level using the observational approach is slightly smaller.

4.3. Inverse of Background Error Covariance Using SVD Method

[23] The realistic treatment of background errors raises numerical issues, such as how to invert B . Using the property of Kronecker product [Horn and Johnson, 1991], B^{-1} can be written as

$$B^{-1} = (X \otimes Y \otimes Z \otimes C)^{-1} = X^{-1} \otimes Y^{-1} \otimes Z^{-1} \otimes C^{-1} \quad (12)$$

Although it is straightforward to directly invert X , Y , Z , and C as all the matrices have full rank and small sizes, it is error-prone to compute the matrix inverse for ill-conditioned matrices. For instance, [Sun and Crook, 2001] calculated the matrix inverse using singular value decomposition (SVD) and found the correlation length scale cannot be greater than four times the grid spacing in order to avoid the ill-conditioning problem. Here we propose to use SVD on the matrices, but truncate the singular vectors that are associated with small singular values to approximate the original matrices.

[24] Using SVD, a general $m \times n$ matrix A can be written as

$$A = U \Sigma V^T \quad (13)$$

where Σ is an $m \times n$ matrix which is zero except for its $\min(m, n)$ diagonal elements, U is an $m \times m$ orthogonal matrix, and V is an $n \times n$ orthogonal matrix. For the

Table 6. Model Bias and RMS Error for Case 9, Calculated Against Each Observation Platform^a

Error	AIRNOW	DC3	MOZ-FN	MOZ-NF	P3	AIRMAP	DC8-In	DC8-Li	RHODE	RONBR
Bias	0.7	-5.1	-5.3	-14.5	-4.8	-4.8	-4.5	-4.4	-4.0	4.1
RMS	14.1	15.8	12.2	19.3	11.0	11.1	11.7	11.2	4.9	14.3

^aUnit is ppbv. See Table 1 for descriptions of the observations.

symmetric matrices X , Y , Z , and C , equation (13) can be simplified as

$$A = U\Sigma U^T \quad (14)$$

The diagonal elements of Σ are the singular values of Σ . The singular values σ_i are positive for positive definite matrices. They are arranged in the descending order, i.e., $\sigma_1 \geq \sigma_2 \cdots \sigma_n > 0$. The columns of U are the corresponding singular vectors. Then it is easy to get

$$A^{-1} = U\Sigma^{-1}U^T \quad (15)$$

where the only nonzero elements of Σ^{-1} are the diagonal ones and they are $\frac{1}{\sigma_1}, \frac{1}{\sigma_2}, \dots, \frac{1}{\sigma_n}$. The small singular values are

the sources of instability and they make the matrix-vector multiplication $A^{-1}b$ extremely sensitive to the perturbation of the vector b . It has been proven that A_p^+b is the minimum norm solution that minimizes $\|A_p^+x - b\|$, which is called truncated singular value decomposition (TSVD) regularization [Gwak and Masada, 2004; Xu, 1998; Hansen et al., 1992]. p denotes the rank of the matrix A_p that approximates A .

$$A_p = U\Sigma_p U^T \quad (16)$$

$$A_p^+ = U\Sigma_p^+ U^T \quad (17)$$

where Σ_p is the diagonal matrix after setting $\sigma_{p+1}, \dots, \sigma_n$ to zero. Σ^+ is a diagonal matrix, with the diagonal elements as $\frac{1}{\sigma_1},$

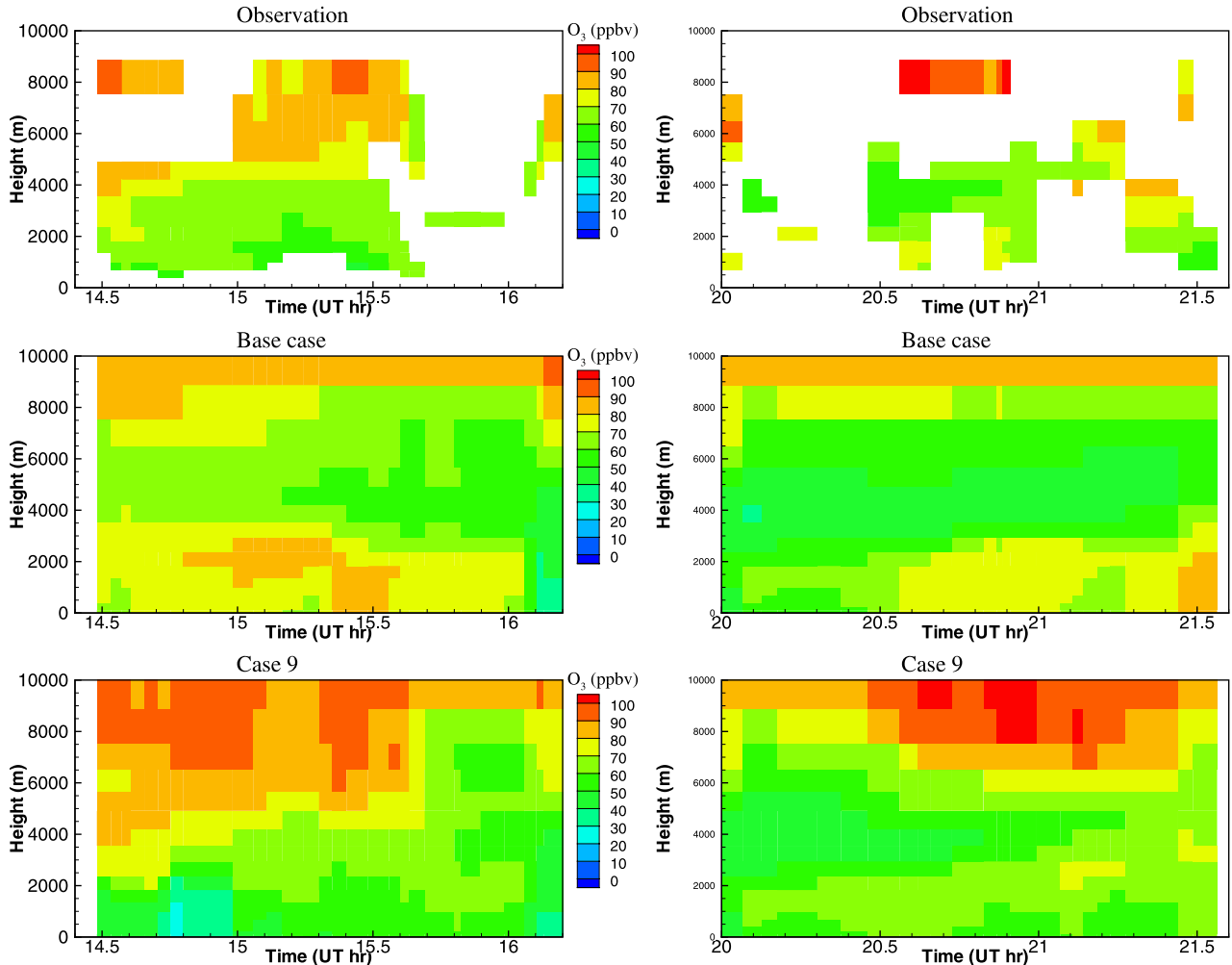


Figure 13. (top) DC-8 lidar ozone observations and the corresponding model predictions by (middle) the base case and (bottom) case 9. Lidar observations have been reduced according to model resolutions, both in time and space.

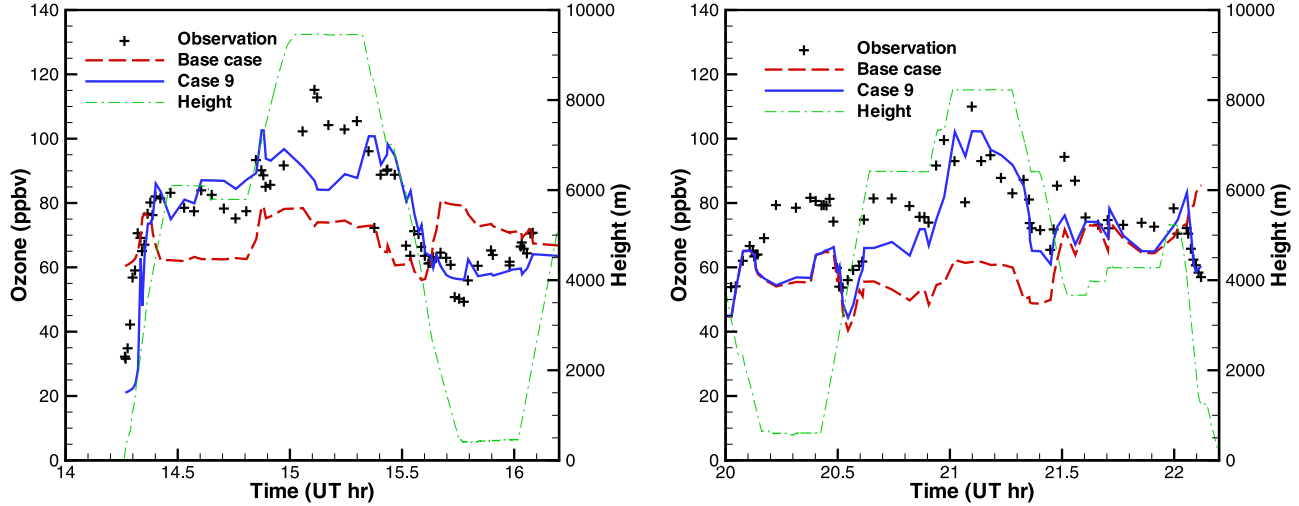


Figure 14. DC-8 in situ ozone observations and the corresponding model predictions by the base case and case 9. Observations have been reduced according to model resolutions, both in time and space.

$\frac{1}{\sigma_2}, \dots, \frac{1}{\sigma_p}, 0, \dots, 0$. With TSVD regularization, B^{-1} is thus approximated by

$$B^{-1} = X_p^+ \otimes Y_p^+ \otimes Z_p^+ \otimes C_p^+ \quad (18)$$

where p may be different for matrices X , Y , and Z . Here p is picked to have the final matrix condition number smaller than 100. Table 2 shows the maximum and minimum singular values and condition numbers of X , Y , and Z , as well as the truncation rank p used in TSVD regularization. It demonstrates the severely ill-conditioning of Z . Without regularization, the direct inverse of Z results in very large background term in equation (3) and that makes the minimization process stop. Figure 8 shows Z_q , as well as Z , which is used to approximate the vertical correlation obtained through the NMC approach, shown in Figure 4. The maximum change of the correlation coefficients represented by elements of Z and Z_p is found to be 0.0073. This implies that such truncation does not change the represented correlation structure, but only removes the noises from the correlation matrix.

[25] The Kronecker products in equation (18) are implemented by applying the X_p^+ , Y_p^+ , Z_p^+ , and C_p^+ subsequently in three different directions, and at each grid point between different species. In the following applications, we take square root of X_p^+ , Y_p^+ , and Z_p^+ matrices, apply them in three directions before applying C_p^+ , and then use the square root matrices in a reverse order.

5. Data Assimilation Results

5.1. Base Case Run

[26] The STEM-predicted ozone distribution without assimilation provides the base conditions for the analysis. The initial and boundary conditions were provided from a STEM simulation at the same resolution, but using a large continental domain [Tang et al., 2007]. The wind fields at 1600 UT and 2000 UT are shown at two different heights, 990 m and 3553 m, in Figure 9. There is not much difference between 1600 UT to 2000 UT, but the flow

fields at the two heights vary significantly. Over land the wind was mainly westerly. The winds were light in the New England area at low altitudes, which makes the ozone production to be largely determined by the local emission.

[27] Table 3 lists the performance of the forward model predictions as evaluated by the observations. The root mean square (RMS) errors range from 13.4 to 26.3 ppbv, with a positive bias for the predictions of surface ozone. This was a general finding of seven different CTMs used to forecast surface ozone during ICARTT [McKeen et al., 2005], including the STEM model. This is shown by the 15.3 ppbv positive bias in the predictions at the AIRNOW surface sites. An over prediction was consistently found in the base run for ozone measurements below 3 km (from aircraft and ozonesondes). In contrast, ozone predictions above 4 km were biased low. These values are significantly influenced

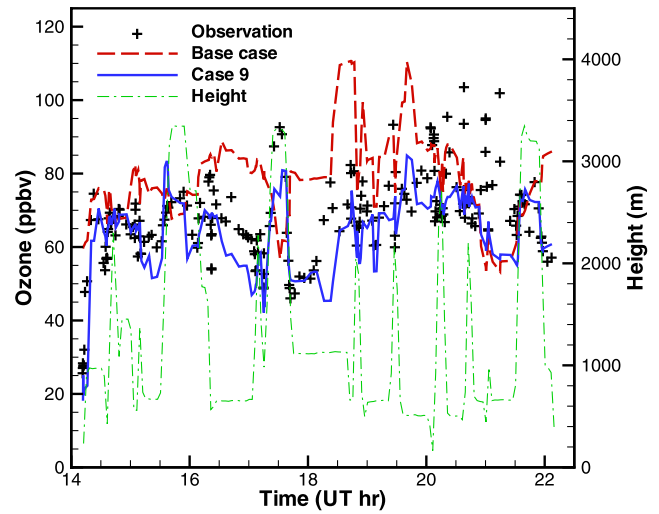


Figure 15. P3 ozone observations and the corresponding model predictions by the base case and case 9. Observations have been reduced according to model resolutions, both in time and space.

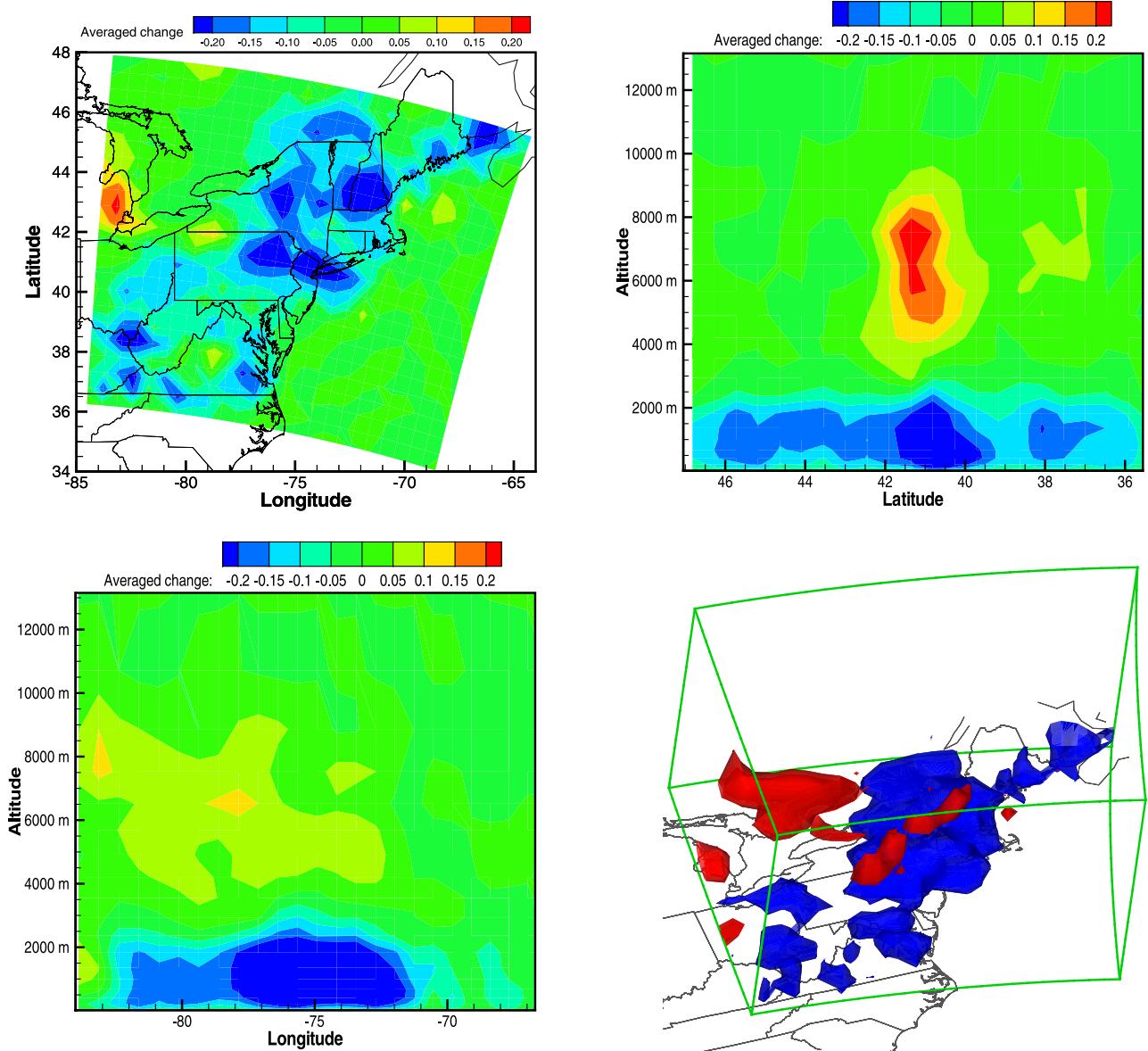


Figure 16. Relative changes of initial O_3 concentration. Averaged values are shown in top, west, and south views. Two isosurfaces of the initial O_3 concentration changes (red indicates 20% increase; blue indicates 20% decrease) are shown in the 3-D plots. The relative changes are based on case 9 over the base case and normalized by average concentrations on each level.

by the boundary conditions from the global model used by the STEM as discussed by [Tang *et al.*, 2007]. These differences will be discussed in more detail later. The bias and RMS values are smaller for the P3 and DC-8 aircraft observation. The effect of model resolution is most pronounced for the surface predictions and not so pronounced for the other data sets. Forward model predictions using a 12 km grid reduced the predicted mean ozone levels by 3 ppbv for the P3 observations below 1 km.

[28] The standard deviation of the combined background and observational errors is

$$E = \sqrt{E_B^2 + E_O^2} = \sqrt{10^2 + 8^2} \approx 12.8 \text{ ppbv}. \quad (19)$$

This is an estimate of the expected model performance. This value can be reduced either by improving the model performance at the current resolution, thus decreasing E_B , or by increasing the model resolution, thus decreasing the representative error, the major component of E_O . It should be noted that the previously obtained ratio between E_B and E_O cannot be directly applied to other models, which probably have different E_B values. For the same model, the change of resolution will affect both E_B and E_O .

[29] Comparisons between the base case model predictions and the observations are shown in Figures 10–12. In general the ozone predictions show high positive biases below ≈ 3 km and high negative bias above ≈ 4 km. The analyses after assimilating all observations are also shown. These results will be discussed in section 5.3.

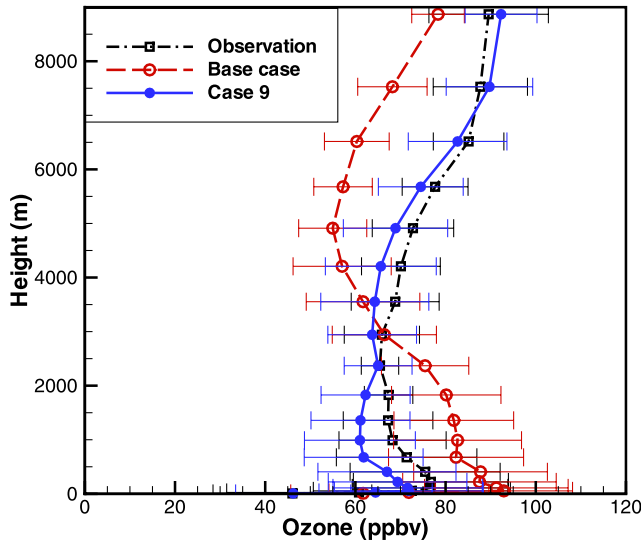


Figure 17. Domain-averaged vertical profiles (with standard deviation) of the ozone observations and the corresponding predictions before (base case) and after assimilation of all observations (case 9).

5.2. Information Content

[30] Eight different data assimilation tests were performed to assess the impact on the assimilation results of the different observation sets. This is an important issue in the design of observing systems to support chemical data assimilation. Basic questions that arise include: do we get a bigger impact by increasing spatial or temporal samples? or by adding information near or above the surface?

[31] The cases are listed in Table 4. Table 5 shows the impact on the predictions after assimilation. For the majority of the cases, assimilating observations improves the model predictions as determined by the withheld observations, and quantified by the reduced RMS errors (shown as negative RMS error changes in Table 5). Exceptions are the increases in RMS errors for the MOZ-NF (MOZAIC flight, New York–Frankfurt) predictions for case 1 and case 8, the MOZ-FN (MOZAIC flight, Frankfurt–New York) predictions after assimilating AIRMAP observations (case 5), and DC-8 lidar predictions after assimilating DC3 observations (case 2). Among them, the only significant RMS error increase (>0.1 ppbv) is on MOZ-NF after assimilating AIRNOW observations (case 1). It is likely that the MOZAIC flight sampled more polluted air than the $60\text{ km} \times 60\text{ km}$ grid cell average. On the other hand, the base case mostly overestimates the ground ozone observations, as discussed in section 5.1. The small RMS errors are probably due to the combinations of these two factors and they are likely to go up if the overprediction at the ground level is mitigated.

[32] It is seen that assimilating AIRNOW observations (case 1) helps to reduce the model RMS errors against AIRMAP, DC3, and P3 by 6.7, 6.0, and 5.8 ppbv respectively. Observations by DC-8 lidar, P3, and DC3 also show significant positive effects on model results when assimilated in cases 7, 4, and 2. Cases 5 and 8 have the smallest effect to improve the model results due to the limited spatial

coverage of the AIRMAP sites and the ozonesonde locations. Case 6 shows more improvement than case 4 as the DC-8 covers a larger area within the domain.

[33] The observation number after performing averaging inside the four-dimensional grid cells is a good indication of the information content of the observations for each platform. As the observation numbers of AIRNOW, DC-8 lidar, DC3 lidar, and P3 listed in Table 4 are larger than the number of observations from the other platforms, they provide greater impact in improving the model predictions when assimilated. Although the observation number for AIRMAP (128) is close to that of P3 (208), the effect of AIRMAP is smaller because of the limited spatial coverage (both horizontally and vertically). Note that the information content also depends on the model resolution. For instance, the DC3 lidar generated a vertical profile every 10 s, which has 85 data points with a vertical resolution of 90 m. Such information cannot be fully utilized with a 60 km grid. It will bring much more information to a smaller domain with higher spatial and temporal resolutions.

5.3. Final Analysis

[34] A final analysis is obtained after all the observations are assimilated. It is listed as case 9 in Tables 4 and 5. Table 5 shows that the observations from all platforms can be successfully assimilated simultaneously, and that the fit between predictions and observations is generally better than when the observations from each individual platform are assimilated separately. The exception is again for MOZ-NF, for which the RMS error increases by 4.0 ppbv. The reason is discussed in section 5.1. The model biases and RMS errors of the final analysis are listed in Table 6. Except for MOZ-FN, the largest model bias is -5.3 ppbv for MOZ-FC, and the largest model RMS error is 15.8 ppbv for DC3 lidar, which is comparable to the expected model performance, $E \approx 12.8$ ppbv, calculated in equation (19).

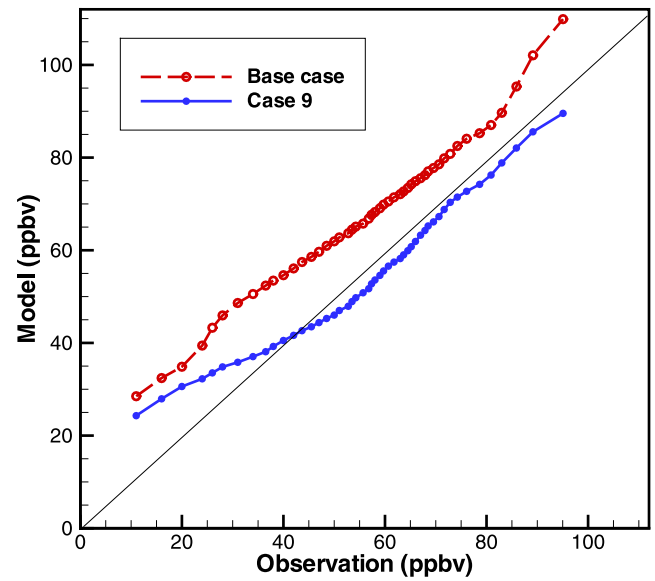


Figure 18. Quantile-quantile plots of the ozone observations (using all data) versus the corresponding predictions, for the base case and case 9. The quantile increment is 2%; that is, quantiles of 2%, 4%, 96%, 98% are shown.

Table 7. Average Model Prediction Changes After Assimilating Ozone Measurements From All Platforms (Case 9 Over the Base Case), Normalized by Average Concentrations on Each Level Before Taking Domain Average^a

Time	O ₃	NO	NO ₂	CO	HCHO	ACET	ARO1	ARO2	PAN	PAN2	OH
1600 UT	-0.061	0.136	0.029	0.000	0.024	0.000	-0.001	-0.001	-0.027	-0.036	0.005
2000 UT	-0.045	0.071	0.032	0.000	0.018	0.000	-0.001	0.001	-0.027	-0.049	0.005
2400 UT	-0.040	0.029	0.022	0.000	0.014	0.000	-0.002	-0.002	-0.028	-0.053	0.012

^aACET, acetone; ARO1, aromatics with kOH < 2×10^4 ppm⁻¹min⁻¹; ARO2, aromatics with kOH > 2×10^4 ppm⁻¹min⁻¹; PAN, peroxy acetyl nitrate; PAN2, PPN (peroxypropionyl nitrate) and other higher alkyl PAN analogues.

[35] The comparisons between predictions of case 9 and the base case, as well as observations are shown in Figures 10–12. Figure 10 shows predicted surface ozone at 2000 UT by the base case and the final analysis, along with observations by AIRNOW and AIRMAP. While the base case overpredicted ozone at many locations, results from the final analysis match most observations well. There is little change in predictions where there are no measurements such as the southeast corner of the domain. The time series of ozone concentrations at AIRMAP locations in Figure 11 show significant improvement in the final analysis at two locations (AIRMAPCS and AIRMAPTF), but has little change over the base case for Appledore Island (AIRMAPIS) location. At Mount Washington Observatory location (AIRMAPMWO), the ozone predictions change from overprediction for the base case to “underprediction” for the final analysis. The “underprediction” is probably due to bias of the measurements. According to the notes provided with the data, the ozone measurements were strongly impacted by exhaust from a generator on site and the cog railway which runs from late April/early May to late October/early November.

[36] Ozone profiles by the two ozonesondes (RHODE and RONBR), and corresponding model predictions by the base case and case 9 are shown in Figure 12. The profiles clearly indicate that the model overpredicted ozone below 3000 m, but underpredicted ozone above the height for the base case run. Ozone at the high altitudes is mainly due to long-range transport. For regional CTMs, predictions are greatly affected by the boundary conditions [Tang *et al.*, 2007]. Ozone at the low altitudes is mostly impacted by the local emissions. Although both boundary conditions and emission inventories are kept the same as the base case, the adjustment of initial ozone concentration is still able to emulate such effects in a short period. Results of the final analysis after assimilating the ozone observations show that both the underpredictions at high altitudes and overpredictions at low altitudes are largely remedied.

[37] Figure 13 shows the “curtain plots” (continuous profiles) of ozone measured by a lidar on board DC-8, along with their model counterparts for the base case and case 9. The base case again overpredicts observations by

DC-8 lidar under 3000 m and underpredicts ozone at higher altitudes. After the data assimilation, significant improvements are found in all regions.

[38] Figures 14 and 15 show the in situ ozone measurements by DC-8 and P3, respectively. Part of the DC-8 flight is out of the domain as shown in Figure 2. In the first part of the DC-8 flight, the base case overpredicts ozone above 4000 m and underpredicts below 4000 m. The final analysis is effectively improved in both regions. For the second part of the DC-8 flight, significant improvement after assimilation is seen during 2030–2130 UT, when the flight is above 4000 m. There is little change made by the data assimilation before 2030 UT and after 2130 UT. Figure 2 shows that the beginning of the second part of the DC-8 flight is at the west boundary of the current domain, which is a in-flow boundary, indicated by the wind fields shown in Figure 9. With the same in-flow boundary conditions used for both the base case and case 9, the ozone predictions cannot be improved by only adjusting the initial conditions. On the other hand, there is a good agreement between the base case predictions and DC-8 In Situ measurements after 2130 UT. The final analysis still sees improvement after 2200 UT. Predictions on the P3 flight measurements by the final analysis improves significantly over the base case, as demonstrated by Figure 15. However several high ozone values (>90 ppbv) were observed, but are not present in model results of case 9.

[39] The assimilation of all the various ozone observations allows us to demonstrate the impact of data assimilation on the generation of a reanalysis field. This is similar to meteorological reanalysis where an optimal field consistent with observations is generated. The relative changes of the initial ozone concentrations after assimilating the observations of multiple platforms are shown in Figure 16. Decreases of initial ozone are seen below 2000 m, and over most of the land area in the domain. This is consistent with a separate analysis of the STEM prediction with ICARTT observations which indicates that the NO_x and some VOC (volatile organic compounds) emissions are overestimated with the NEI 2001 inventory [Mena-Carrasco *et al.*, 2007]. There is a region between 4000–8000 m, and close to the west boundary, that sees increases of initial ozone concen-

Table 8. RMS Mean of Model Prediction Changes After Assimilating Ozone Measurements From All Platforms (Case 9 Over the Base Case), Normalized by Average Concentrations on Each Level Before Taking Domain RMS

Time	O ₃	NO	NO ₂	CO	HCHO	ACET	ARO1	ARO2	PAN	PAN2	OH
1600 UT	0.168	0.788	0.101	0.000	0.059	0.003	0.033	0.111	0.075	0.093	0.044
2000 UT	0.129	0.616	0.138	0.001	0.045	0.005	0.101	0.210	0.080	0.121	0.042
2400 UT	0.114	0.268	0.108	0.001	0.036	0.004	0.057	0.109	0.078	0.124	0.050

Table 9. Maximum Model Prediction Change After Assimilating Ozone Measurements From All Platforms (Case 9 Over the Base Case), Normalized by Average Concentrations on Each Level^a

Time	O ₃	NO	NO ₂	CO	HCHO	ACET	ARO1	ARO2	PAN	PAN2	OH
1600 UT	-0.827	24.899	-2.992	0.006	0.371	-0.073	1.693	7.655	-0.950	-0.936	-0.696
2000 UT	-0.682	21.948	5.105	0.015	0.256	-0.129	4.070	10.170	-1.394	-1.483	-0.749
2400 UT	-0.613	8.736	3.099	0.011	0.244	-0.113	1.757	3.756	-1.172	-1.219	-0.504

^aMaximum change is based on the magnitude of the normalized changes.

trations. This suggests that the boundary conditions require adjustment (which can be added to the 4D-Var control variables).

[40] Figure 17 shows the domain-averaged vertical profiles (with standard deviation) constructed using the observations and the corresponding predictions for case 9 and the base case. It clearly shows that the model biases both below and above 3000 m are substantially reduced for case 9. The predicted values for case 9, now show a negative bias at low to midaltitudes and a positive bias at high altitudes. Assessed with all the observations throughout the boundary layer and mid troposphere, the model bias is reduced from 11.3 ppbv for the base case to -1.5 ppbv for case 9. A reduction of 10.3 ppbv in RMS error is also seen. The model biases and RMS errors of the final analysis against the individual platforms are listed in Table 6.

[41] Figure 18 gives the quantile-quantile (q-q) plots of the ozone observations versus the corresponding predictions, for the base case and case 9. Each point in a quantile-quantile plot shows the values from two data sets that has the same quantile, i.e., the fraction of data points that fall below the given value. The q-q plot of the base case clearly

shows the predictions are biased high overall. After assimilation, case 9 generates a predicted ozone field that has a very similar population distribution as the observations. The q-q plot of case 9 also indicates that the model has difficulty to generate low ozone concentrations (<20 ppbv) in the data assimilation time period. This is largely due to the coarse model resolution.

[42] As the chemical species are closely connected through various photochemical reactions, the adjustment of initial ozone concentrations will affect the predictions of other species. The impact of the assimilation of ozone observations on the predictions of selected chemical species are listed in Tables 7–9. The largest impacts are found for NO where the RMS mean of NO prediction changes are 78.8% at 1600 UT (1200 EDT), and then decreases to 26.8% at 2400 UT (2000 EDT). Figure 19 shows the isosurfaces of 100% increase of predicted NO concentration at 1600 UT. It is the data-rich region that is more affected by assimilation than the other areas. This highly impacted region extends to ≈3000 m in height. Note that NO predictions are increased over almost the whole domain, which is also indicated by the large average change in

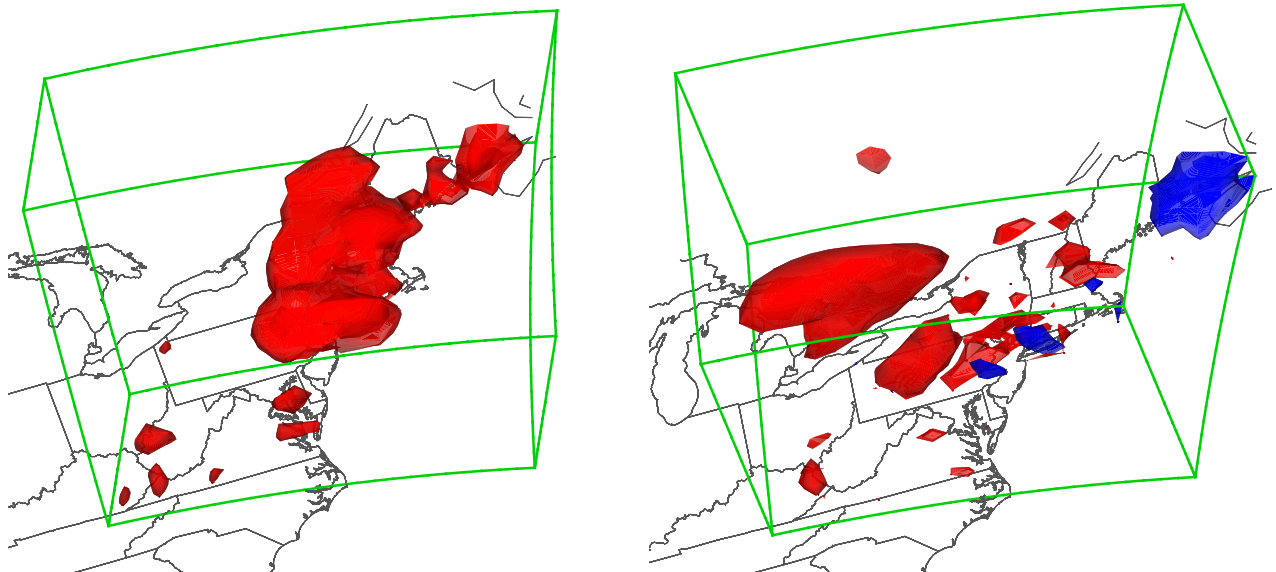


Figure 19. Relative changes of predicted (left) NO and (right) OH concentrations at 1600 UT. Isosurfaces of 100% increase for NO, 5% increase (red) and 5% decrease (blue) for OH are shown. The relative changes are based on case 9 over the base case and normalized by average concentrations on each level.

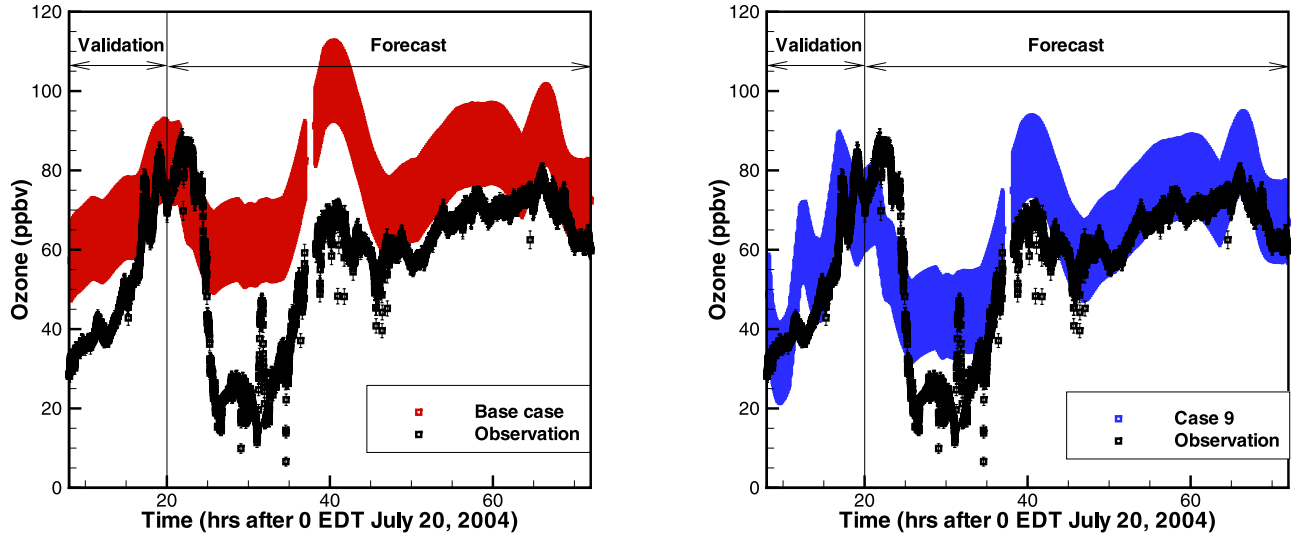


Figure 20. UV absorbance ozone measurements on NOAA research vessel *Ronald H. Brown* and corresponding model predictions by (left) the base case and (right) case 9. Measurement uncertainties ($+/- (2\% + 1 \text{ ppbv})$) are shown as error bars. Model prediction uncertainties are given as ($+/- 10 \text{ ppbv}$), indicated by a band width of 20 ppbv.

Table 7. Figure 19 also shows the isosurfaces of $\pm 5\%$ change in OH at 1600 UT, and displays a different distribution than that of NO. Although ozone is often highly correlated with CO, the changes in initial ozone concentrations had little effect on the CO predictions, with the maximum change as 1.1%, reflecting that the feedbacks operate at a much longer timescale than studied here.

[43] In addition to the observations that are assimilated in case 9, there are more independent ozone measurements during the time period. Onboard the NOAA research vessel *Ronald H. Brown* (*Ron Brown*), both Chemiluminescence and UV absorbance instruments were used to sample ozone at ~ 15 meters above waterline. The two data sets are consistent with each other, but the uncertainty of UV absorbance ozone measurements ($+/- (2\% + 1 \text{ ppbv})$) is smaller than that of chemiluminescence data ($+/- (2\% + 3 \text{ ppbv})$). The ship positions between 1200 UT on 20–22 July 2004 are given in Figure 2. Figure 20 shows the UV absorbance ozone measurements and the corresponding model predictions by the base case and case 9. In the data assimilation time window, the UV absorbance ozone measurements serve as another validation data set. It is clearly seen that after assimilation the model predictions for the *Ron Brown* better match the observations. More importantly, the positive effect continues beyond the data assimilation time window (even out to 48 hours). This demonstrates the potential of improving air quality forecasts by chemical data assimilation. However improved ozone forecasts will require the assimilation of precursor species, and the inclusion of emissions and boundary conditions as control variables. This is a subject of a future paper.

6. Summary and Discussion

[44] The ICARTT experiments produced comprehensive observation data sets and intense modeling applications upon which to study important aspects of data assimilation.

A key element is the characterization of errors. The model error correlation was constructed using the NMC approach. It is implemented into a 4D-Var regional chemical data assimilation system with a truncated SVD regularization method. The observational (Hollingworth-Lönnberg) method was used to calculate the weighting between observations and the model background in 4D-Var. It should be noted that the increase of the computational time is minimal using the current approach, compared to using a diagonal matrix for the background error covariance. The weighting between the model and observations in determining the final optimal analysis depends on both the background and observational error covariance matrices, which were objectively approximated in the current application.

[45] Ozone observations by different platforms during the ICARTT field experiment were assimilated into the regional CTM. It was found with little exception that assimilating observations from each individual platform improved the model predictions against the withheld observations. The information content of the observations depends on the model resolution and it can be approximated by the number of four-dimensional (in space and time) grid cells that the observations spread over. A final analysis where all the observations by the different platforms were simultaneously assimilated, resulted in a reduction in bias to -1.5 ppbv from 11.3 ppbv for the base case without assimilation. A reduction of 10.3 ppbv in RMS error was also seen. In addition, the potential of improving air quality forecasts with chemical data assimilation was demonstrated by a case where the near surface ozone predictions better match observations out to 48 hours after assimilation.

[46] In the current data assimilation experiments, only initial ozone concentrations were adjusted. This limits the effect of the data assimilation (especially for forecasts) as model predictions at some locations are more affected by the boundary conditions or emission inventories. Adjusting initial concentrations of other species will probably

help to improve the model predictions and air quality forecasts. In addition, the benefit of assimilating satellite observations and measurements of additional species need to be exploited. These issues will be addressed in future papers.

[47] **Acknowledgments.** The authors gratefully thank NASA GTE and ACMAP Programs, NOAA Climate and Global Change Program, and the National Science Foundation ITR Program for their support. The authors acknowledge for their strong support the European Commission, Airbus, and the airlines (Lufthansa, Austrian, and Air France) who carry free of charge the MOZAIC equipment and perform the maintenance since 1994. MOZAIC is supported by INSU-CNRS (Institut National des Sciences de l'Univers—Centre National de la Recherche Scientifique, France) and by FZJ (Forschungszentrum Jülich, Germany).

References

- Byrd, R., P. Lu, and J. Nocedal (1995), A limited memory algorithm for bound constrained optimization, *SIAM J. Sci. Stat. Comput.*, **16**(5), 1190–1208.
- Carmichael, G. R., D. N. Daescu, A. Sandu, and T. Chai (2003), Computational aspects of chemical data assimilation into atmospheric models, in *Computational Science—ICCS 2003, Lecture Notes in Computer Science, IV*, pp. 269–278, Springer, Berlin.
- Carter, W. (2000), Documentation of the SAPRC-99 chemical mechanism for VOC reactivity assessment, *Tech. Rep.* 92-329, Calif. Air Resour. Board Contract, Sacramento.
- Chai, T., G. R. Carmichael, A. Sandu, Y. Tang, and D. N. Daescu (2006), Chemical data assimilation of transport and chemical evolution over the Pacific (TRACE-P) aircraft measurements, *J. Geophys. Res.*, **111**, D02301, doi:10.1029/2005JD005883.
- Courtier, P. (1997), Dual formulation of four-dimensional variational assimilation, *Q. J. R. Meteorol. Soc.*, **123**(544B), 2449–2462.
- Daescu, D. N., and G. R. Carmichael (2003), An adjoint sensitivity method for the adaptive location of the observations in air quality modeling, *J. Atmos. Sci.*, **60**, 434–449.
- Daescu, D. N., A. Sandu, and G. R. Carmichael (2003), Direct and adjoint sensitivity analysis of chemical kinetic systems with KPP: II—Numerical validation and applications, *Atmos. Environ.*, **37**, 5097–5114.
- Daley, R. (1991), *Atmospheric Data Analysis*, 457 pp., Cambridge Univ. Press, New York.
- Elbern, H., and H. Schmidt (1999), A 4D-Var chemistry data assimilation scheme for Eulerian chemistry transport modeling, *J. Geophys. Res.*, **104**(D15), 18,583–18,598.
- Elbern, H., and H. Schmidt (2001), Ozone episode analysis by four-dimensional variational chemistry data assimilation, *J. Geophys. Res.*, **106**(D4), 3569–3590.
- Elbern, H., H. Schmidt, and A. Ebel (1997), Variational data assimilation for tropospheric chemistry modeling, *J. Geophys. Res.*, **102**(D13), 15,967–15,985.
- Elbern, H., H. Schmidt, O. Talagrand, and A. Ebel (2000), 4D-variational data assimilation with an adjoint air quality model for emission analysis, *Environ. Modeling Software*, **15**, 539–548.
- Fisher, M., and D. J. Lary (1995), Lagrangian four-dimensional variational data assimilation of chemical species, *Q. J. R. Meteorol. Soc.*, **121**, 1681–1704.
- Gao, J., M. Xue, K. Brewster, and K. K. Droegemeier (2004), A three-dimensional variational data analysis method with recursive filter for doppler radars, *J. Atmos. Oceanic Technol.*, **21**(3), 457–469.
- Grell, G. A., J. Dudhia, and D. R. Stouffer (1994), A description of the fifth-generation Penn State/NCAR mesoscale model (MM5), *Tech. Rep.*, NCAR/TN – 398 + STR, Natl. Cent. for Atmos. Res., Boulder, Colo.
- Gwak, K.-W., and G. Y. Masada (2004), Regularization embedded nonlinear control designs for input-constrained and ill-conditioned thermal system, *Trans. ASME*, **126**(3), 574–582, doi:10.1115/1.1789973.
- Hansen, P. C., T. Sekii, and H. Shibahashi (1992), The modified truncated SVD method for regularization in general-form, *SIAM J. Sci. Stat. Comput.*, **13**(5), 1142–1150.
- Hoelzemann, J. J., H. Elbern, and A. Ebel (2001), SAS and 4D-var data assimilation for chemical state analysis by urban and rural observation sites, *Phys. Chem. Earth, Part B*, **26**(10), 807–812.
- Hollingsworth, A., and P. Lönnberg (1986), The statistical structure of short-range forecast errors as determined from radiosonde data. Part I: The wind field, *Tellus, Ser. A*, **38**, 111–136.
- Hong, S.-Y., and H.-L. Pan (1996), Nonlocal boundary layer vertical diffusion in a medium-range forecast model, *Mon. Weather Rev.*, **124**(10), 2322–2339.
- Horn, R. A., and C. R. Johnson (1991), *Topics in Matrix Analysis*, Cambridge Univ. Press, New York.
- Horowitz, L. W., et al. (2003), A global simulation of tropospheric ozone and related tracers: Description and evaluation of MOZART, version 2, *J. Geophys. Res.*, **108**(D24), 4784, doi:10.1029/2002JD002853.
- Lorenc, A. C. (1997), Development of an operational variational assimilation scheme, *J. Meteorol. Soc. Jpn.*, **75**(1B), 229–236.
- Mareno, A., et al. (1998), Measurement of ozone and water vapour by Airbus in-service aircraft: The MOZAIC airborne programme, an overview, *J. Geophys. Res.*, **103**(D19), 25,631–25,642.
- McKeen, S., et al. (2005), Assessment of an ensemble of seven real-time ozone forecasts over eastern North America during the summer of 2004, *J. Geophys. Res.*, **110**, D21307, doi:10.1029/2005JD005858.
- Mena-Carrasco, M., et al. (2007), Improving ozone modeling during the ICARTT period using NEI 2001 and kriging, *J. Geophys. Res.*, doi:10.1029/2006JD007762, in press.
- Nédélec, P., et al. (2003), An improved infrared carbon monoxide analyser for routine measurements aboard commercial Airbus aircraft: Technical validation and first scientific results of the MOZAIC III programme, *Atmos. Chem. Phys.*, **3**, 1551–1564.
- Parrish, D., and J. Derber (1992), The National Meteorological Center's spectral statistical-interpolation analysis system, *Mon. Weather Rev.*, **120**(8), 1747–1763.
- Pfister, G., P. G. Hess, L. K. Emmons, J.-F. Lamarque, C. Wiedinmyer, D. P. Edwards, G. Pétron, J. C. Gille, and G. W. Sachse (2005), Quantifying CO emissions from the 2004 Alaskan wildfires using MOPITT CO data, *Geophys. Res. Lett.*, **32**, L11809, doi:10.1029/2005GL022995.
- Purser, R. J., W.-S. Wu, D. F. Parrish, and N. M. Roberts (2003a), Numerical aspects of the application of recursive filters to variational statistical analysis. Part I: Spatially homogeneous and isotropic Gaussian covariances, *Mon. Weather Rev.*, **131**(8), 1524–1535.
- Purser, R. J., W.-S. Wu, D. F. Parrish, and N. M. Roberts (2003b), Numerical aspects of the application of recursive filters to variational statistical analysis. Part II: Spatially inhomogeneous and anisotropic general covariances, *Mon. Weather Rev.*, **131**(8), 1536–1548.
- Sandu, A., D. N. Daescu, and G. R. Carmichael (2003), Direct and adjoint sensitivity analysis of chemical kinetic systems with KPP: I—Theory and software tools, *Atmos. Environ.*, **37**, 5083–5096.
- Sandu, A., D. Daescu, G. R. Carmichael, and T. Chai (2005), Adjoint sensitivity analysis of regional air quality models, *J. Comput. Phys.*, **204**(1), 222–252.
- Singh, H. B., W. H. Brune, J. H. Crawford, and D. J. Jacob (2006), Overview of the summer 2004 Intercontinental Chemical Transport Experiment—North America (INTEX-A), *J. Geophys. Res.*, **111**, D24S01, doi:10.1029/2006JD007905.
- Sun, J. Z., and N. A. Crook (2001), Real-time low-level wind and temperature analysis using single WSR-88d data, *Weather Forecasting*, **16**, 117–132.
- Tang, Y., et al. (2003), Impacts of aerosols and clouds on photolysis frequencies and photochemistry during TRACE-P: 2. Three-dimensional study using a regional chemical transport model, *J. Geophys. Res.*, **108**(D21), 8822, doi:10.1029/2002JD003100.
- Tang, Y., et al. (2004), Multiscale simulations of tropospheric chemistry in the eastern Pacific and on the U.S. West Coast during spring 2002, *J. Geophys. Res.*, **109**, D23S11, doi:10.1029/2004JD004513.
- Tang, Y., et al. (2007), Influence of lateral and top boundary conditions on regional air quality prediction: A multiscale study coupling regional and global chemical transport models, *J. Geophys. Res.*, **112**, D10S18, doi:10.1029/2006JD007515.
- Thouret, V., A. Mareno, J. Logan, P. Nédélec, and C. Grouhel (1998), Comparisons of ozone measurements from the MOZAIC airborne program and the ozone sounding network at eight locations, *J. Geophys. Res.*, **103**(D19), 25,695–25,720.
- Xu, P. L. (1998), Truncated SVD methods for discrete linear ill-posed problems, *Geophys. J. Int.*, **135**(2), 505–514.
- Zhu, C., R. H. Byrd, and J. Nocedal (1997), L-BFGS-B—fortran routines for large scale bound constrained optimization, *ACM Trans. Math. Software*, **23**(4), 550–560.

M. A. Avery and E. V. Browell, NASA Langley Research Center, Hampton, VA 23681, USA.

G. R. Carmichael, T. Chai, and Y. Tang, Center for Global and Regional Environmental Research, University of Iowa, 429 IATL, Iowa City, IA 52246, USA. (tchai@cgrrr.uiowa.edu)

M. Hardesty, Environmental Technology Laboratory, NOAA, Boulder, CO 80305, USA.

J. T. Merrill, Center for Atmospheric Chemistry Studies, Graduate School of Oceanography, University of Rhode Island, Narragansett, RI 02882, USA.

P. Nédélec, Laboratoire d'Aérologie, Centre National de la Recherche Scientifique, F-31400 Toulouse, France.

P. Pilewskie, NASA Ames Research Center, Moffett Field, CA 94035, USA.
A. Sandu, Department of Computer Science, Virginia Polytechnic Institute and State University, Blacksburg, VA 24061, USA.
A. M. Thompson, NASA Goddard Space Flight Center, Greenbelt, MD 20771, USA.

S. Whitlow, Climate Change Research Center, Institute for the Study of Earth, Oceans, and Space, University of New Hampshire, Durham, NH 03824, USA.
E. Williams, Chemical Sciences Division, Earth System Research Laboratory, NOAA, Boulder, CO 80305, USA.